Atomistic simulation of Y-site substitution in multiferroic *h*-$YMnO_3$

Chengguo Zhang, X. Zhang,* Yonghao Sun, and Shuyi Liu

Laboratory of Advanced Materials, Department of Materials Science and Engineering, Tsinghua University, Beijing 100084, People's Republic of China and Beijing National Center of Electron Microscopy, Beijing 100084, People's Republic of China

(Received 15 July 2010; published 15 February 2011)

The interatomic potentials of multiferroic *h*-$YMnO_3$ have been developed, which can reproduce the crystal structure of *h*-$YMnO_3$ quite well. The doping behaviors of a variety of dopants from monovalent to tetravalent ions at the Y site have been systematically investigated by employing atomistic simulation techniques. It is found that Zr^{4+}, Sn^{4+}, Na^{+}, and Ca^{2+} are the favorable dopants to incorporate into *h*-$YMnO_3$ and have an energetic preference for the Y2 site, while Ce^{4+} and Th^{4+} can enter both Y1 and Y2 sites. The structural changes and local polarization caused by these dopants are also investigated. The incorporation of the studied dopants into the Y2 site suppresses the tilting of the MnO_5 polyhedron, while the entrance of these dopants into the Y1 site enhances the tilting, except for Na^{+} and Ca^{2+}. It is also found that Zr^{4+}, Sn^{4+}, Na^{+}, and Ca^{2+} are deleterious dopants for ferroelectric polarization. We also discover that the ferroelectric polarization of *h*-$YMnO_3$ is not driven entirely by electrostatic and size effects, although they have an important effect.

DOI: 10.1103/PhysRevB.83.054104 PACS number(s): 61.72.−y, 77.22.Ej

I. INTRODUCTION

Multiferroics, which possess magnetism and ferroelectricity in the same material simultaneously, have drawn much attention due to their exotic properties and potential applications, such as spintronics, magnetoelectric sensors, etc.[1,2] Among the known multiferroic materials, extensive studies have been performed on hexagonal manganites, especially on the relatively simple hexagonal yttrium manganese oxide (*h*-$YMnO_3$) ($YMnO_3$ also has a relatively unstable orthogonal perovskite structure), which exhibits high ferroelectric transition temperature ($T_c \sim 900$ K) and low antiferromagnetic transition temperature ($T_N \sim 70$ K).[3,4] In this hexagonal structure, there are two inequivalent yttrium positions and four different oxygen sites, while there is only one Mn site in symmetry.[5] The Mn^{3+} ions form MnO_5 bipyramids with three planar oxygen (O3 and O4) and two apical oxygen (O1 and O2) atoms, and this coordination results in a quite different crystal field compared with the perovskite manganites which show Jahn-Teller effects. The yttrium atoms are caged by oxygen and one capping O^{2-} has a substantially larger Y-O bond length than the other seven, thus the yttrium atoms are considered to be sevenfold coordination. Along the *c* direction, the crystal structure is composed of alternative Y^{3+} ions and corner-shared MnO_5 polyhedron layers, as schematically shown in Fig. 1.

It is reported that defects have significant effects on the ferroelectric properties for *h*-$YMnO_3$. A recent study combining transmission electron microscopy and conductive atomic force microscopy revealed that the ferroelectric domain walls and cloverleaf structural antiphase boundaries were mutually locked, and this strong locking resulted in incomplete poling even when large electric fields were applied.[6] Besides, impurities and point defects such as vacancies generated giant changes of the leakage current, which significantly deteriorates the ferroelectric properties.[7]

Cation doping offers opportunities to broaden the variety of the material and tune its properties. Zr^{4+} doping at the Y site could decrease leakage current[8] and suppress both ferroelectric and magnetic ordering drastically.[9] Ce^{4+} has been used to provide electrons for *h*-$YMnO_3$ which turn the Mn^{3+} into Mn^{2+}.[10,11] The substitution of Bi at the Y site reduced growth temperature by more than150 °C, which was attributed to the enhanced surface mobility of adatoms upon Bi doping.[12] It was reported, based on neutron-diffraction data, that Er could enter the two inequivalent yttrium positions, which was detrimental to geometrical frustration effects.[13] Recently, the doping effects of Lu has also been reported by Park *et al.*, however, the site selectivity of the two distinct yttrium positions was not distinguished yet within their experimental resolution.[14] For the Mn-site substitution, electron diffraction and real-space imaging techniques showed that doping of Ti^{4+} in $Y_{1-x}Ti_xMnO_3$ resulted in the paraelectric phase growing up at the expense of the ferroelectric $P6_3cm$ phase around $x = 0.20$ and the paraelectric phase was dominant above $x = 0.30$, which suppressed the ferroelectric property and magnetocapacitance effect ($x > 0.20$).[15] However, the magnetocapacitance enhanced by two orders of magnitude upon doping of Ga^{3+} ions at Mn site.[16,17] Further, the incorporation of Al, Ru, and Zn into the Mn site has been found to reduce the magnetic properties of the Mn triangular network significantly.[18]

Although some of experimental results were given, a systematic understanding of dopant incorporation for *h*-$YMnO_3$ is still lacking. Moreover, it is still elusive how such doping affects the structure and its ferroelectric polarization. The aim of this work is to investigate these issues by use of atomistic simulation techniques. Here, we present our calculated results of a variety of dopants from monovalent to tetravalent ions at the Y site; the effects on structure and ferroelectric polarization are also discussed. This work will be helpful to comprehend the complex doping effects on the local structure in *h*-$YMnO_3$ and design new multiferroics by doping various cations into *h*-$YMnO_3$.

II. COMPUTATIONAL METHODS

The crystal structure of a material at a given temperature and pressure can be predicted by minimizing its free energy.

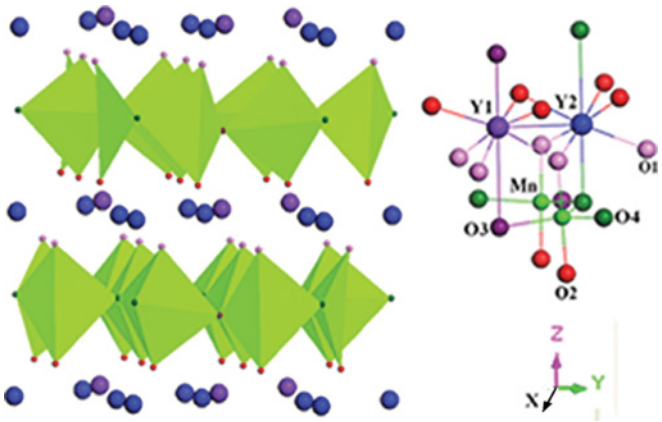

FIG. 1. (Color online) Schematic views of crystallographic structure of hexagonal $YMnO_3$. The polyhedra of YO_7 and MnO_5 are also shown. Note that one capping O^{2-} ion displaces from the caged Y^{3+} significantly larger than the other seven, and thus Y ions are believed to be sevenfold coordination.

The approach is to adjust the cell volume and atomic positions until the net pressure or stress is zero. The pressure P is the derivative of the free energy F with respect to volume V. Thus for hexagonal materials, a pressure corresponding to the derivative of the free energy for each component is calculated, assuming the thermal contribution to the pressure is isotropic:

$$P_j = \frac{1}{V}\frac{dF}{d\varepsilon_j}, \tag{1}$$

where V is the unit cell volume. During the iterative procedure a constant volume energy minimization is performed. Hence each time when the cell volume is modified, all atomic positions are adjusted so that they remain at a potential-energy minimum. Thus by minimizing to constant pressure and including the vibrational component of the free energy, the crystal structure at a given temperature and pressure can be predicted. Details of this technique are available in Ref. 19.

Our calculation is based on the widely used Born model of ionic solids with ions assigned integral charges corresponding to their formal oxidation states.[20] With this model, the lattice energy E can be expressed as

$$E = \frac{1}{2}\sum_{i,j}\left[\frac{q_i q_j}{r_{ij}} + V(r_{ij})\right], \tag{2}$$

where the first item is Coulombic energy introduced by long-range interactions of effective charges, and the second item is the short-range interactions. Short-range interaction used in this work is represented by a Buckingham potential,

$$V(r) = A\exp(-r/\rho) - Cr^{-6}, \tag{3}$$

where the fitting parameters A,ρ are related to the hardness and size of ions, while C represents the van der Waals forces between ions.

To describe the polarization of ions, the shell model[21] is employed. In this model, each atom is represented by a massive core coupled to a massless shell. The interactions between shells are normally restricted to short range denoted via Buckingham potential, while the interaction between the core and corresponding shell is treated as harmonic with a spring constant k and represented by

$$E_v(d_i) = \tfrac{1}{2}kd_i^2, \tag{4}$$

where d_i is the relative displacement of the core and shell of ion i. The free-ion polarization of the shell with charge Y and the core with charge X ($X + Y$ is the formal charge of the ion) can be represented as

$$\alpha = \frac{Y^2}{k}, \tag{5}$$

where the fitting parameter Y is related to the dielectric constant, and the fitting parameter k is the force constant between the core and the shell, which is related to the phonon frequency. The fitting process comprises determination of interatomic potentials by least-squares fitting of calculated results to available experimental properties. The potential parameters A, ρ, and C for cation-oxygen interactions and shell parameters (Y and k) were represented as variables in the fitting procedure. The relaxed fitting procedure can minimize the difference between the calculated and experimental structures and properties with the structure relaxed to zero strain under the symmetry of space group $P6_3cm$ for every evaluation of the sum of squares. The minimization started from the experimental structure in each step to avoid the possibility that the fitting becomes trapped in an undesirable local minimum in either potential or geometry space.

The lattice relaxation about point defects, holes, or dopants was calculated by an implementation of the Mott-Littleton[22] scheme incorporated in the GULP code.[23] In this work, a crystal lattice is partitioned into two regions (regions I and II). Ions immediately surrounding the defect within region I which has a radius of 16.0 Å (about 1400 atoms) relaxed explicitly. Relaxation of such a large number of ions is important for charged defects that introduce long-range electrostatic perturbations and are not easily treated by electronic structure methods such as first-principles calculation. For such a large radius, the calculated defect energies converge and are not sensitive to further expansion of the region any more, with its variation with size of region I less than 0.002 eV/Å. To ensure a smooth transition between regions I and II, an interfacial region IIa is incorporated in which ion displacements are determined via the Mott-Littleton approximation, but in which interactions with ions in region I are calculated by explicit summation. Region IIa extends the radius out to 26.0 Å (about 4300 atoms). The outer region II extends to infinity, with its lattice relaxation treated by quasicontinuum methods, since the defect forces here are relatively weak.

Although the atomistic simulation technique is phenomenological, it has been successfully used for structural simulation of high-temperature superconductors $YBa_2Cu_3O_7$,[24–26] SiO_2,[27] and in ferroelectrics to study superlattices,[28] thin films,[29] and surfaces.[30] An ionic model has been successfully used to calculate the dipole-active optical phonons in $YTiO_3$,[31] lattice dynamics of $SmMnO_3$, $EuMnO_3$, $GdMnO_3$,[32] $YMnO_3$,[33–35] and $LaMnO_3$,[36] charge ordering of $LaMnO_3$.[37] The successful applications give us confidence on our simulation results of $YMnO_3$, nevertheless, it should be cautious to use the ionic model in $ReMnO_3$ (where Re stands for rare earth) since these compounds are not typical ionic materials though

TABLE I. Potential parameters for the hexagonal $YMnO_3$: short-range interaction and shell model parameters (cutoff = 12 Å).

	A (eV)	ρ(Å)	C (eV Å^6)
(a) Short-range interaction			
Y^{3+}—O^{2-}	11335.0177	0.25482	0.0
Mn^{3+}—O^{2-}	879.85946	0.34951	0.0
O^{2-}—O^{2-}	22764.3000	0.14900	43.00
(b) Shell model			
Species	Y (e)	K (eV Å^{-2})	
Y^{3+}	4.577	16.80	
Mn^{3+}	2.10	55.30	
O^{2-}	−2.389	42.0	

they have some ionic attributes, and the simulation results should be checked carefully with the experimental data.

III. RESULTS AND DISCUSSION

A. Interatomic potentials

The interatomic potentials play a key role in computer simulation. Therefore it is necessary to get reliable potential parameters for h-$YMnO_3$. In this work, the potential parameters for h-$YMnO_3$ have been developed by using an empirical method known as the "relaxed" fitting approach, and they are listed in Table I. This potential can reproduce the crystal structure of h-$YMnO_3$ with the differences in lattice parameters between the calculated and experimental data[38] less than 0.2%. The differences in bond lengths between the calculated and experimental data are less than 0.93% except for the bonds Y1-O3 and Y2-O4, which have the largest difference of about 0.1 Å (Table II). Moreover, the calculated bond angles deviate from the corresponding experimental values less than 0.32%, as shown in Table II. The good agreement indicates that the potentials we developed can represent the crystal structures of h-$YMnO_3$.

In order to further assess the validity of our potential model, we calculated the pressure effect on the structure of h-$YMnO_3$ up to a pressure of 7.5 GPa, since most problems to be solved are in a nonequilibrium state. The calculated results are shown in Fig. 2. It is found that as pressure increases the lattice parameters decrease slightly, and the calculated lattice parameter a is in good agreement with the available experimental results while the calculated lattice parameter c has a slight deviation from the experimental data.[39,40] This good agreement confirms that our potentials can be employed for the nonequilibrium state. Besides, we have also checked the dynamical properties of h-$YMnO_3$, such as phonon dispersion curves and infrared-active (IR) phonon frequencies (not shown here). For IR-active mode frequencies, our calculated results agree with the experimental data, and in the phonon-dispersion calculation no imaginary frequencies of vibrational modes have been found, which further indicates that our potential model is stable and reliable. The reliability of our developed potential models via lattice, pressure, and dynamical properties checks provides a valid starting point for the following doping calculation.

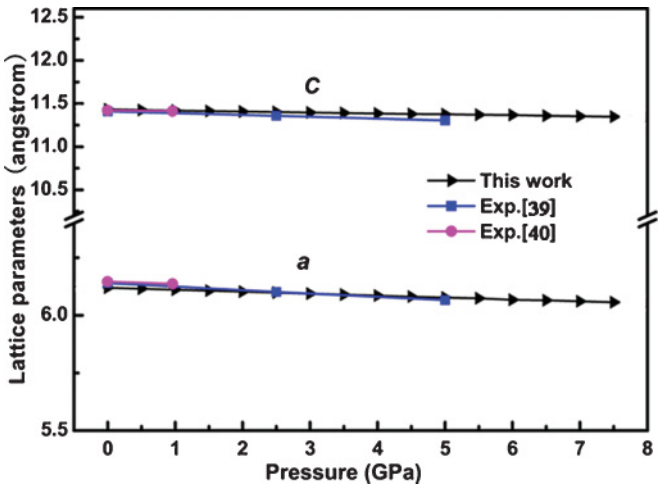

FIG. 2. (Color online) Calculated pressure dependence of lattice parameters a and c, and compared with the experimental data.

TABLE II. Comparison of calculated and experimental structural data for hexagonal $YMnO_3$.

	Experimental	Calculated	Difference
(a) Lattice parameters			
a (Å)	6.12	6.1203	0.01%
c (Å)	11.41	11.4316	0.19%
V (Å^3)	370.10	370.84	0.20%
(b) Interatomic distances (Å)			
Y1-O1	2.2638	2.2682	0.18%
Y1-O2	2.3104	2.2923	0.93%
Y1-O3	2.3162	2.4229	4.6%
Y2-O1	2.2664	2.2670	0.02%
Y2-O2	2.2974	2.2800	0.75%
Y2-O4	2.4611	2.5647	4.2%
Mn-O1	1.8606	1.8637	0.17%
Mn-O2	1.8778	1.8714	0.34%
Mn-O3	2.0495	2.0488	0.03%
Mn-O4	2.0567	2.0558	0.04%
(c) Bond angle (°)			
O1-Mn-O2	179.994	179.950	0.02%
O3-Mn-O4	120.422	120.338	0.07%
Mn-O3-Mn	118.212	118.591	0.32%
Mn-O4-Mn	119.186	119.121	0.05%

B. Y-site substitution

Experimental studies have revealed the possibility of tuning its structure, ferroelectric, and magnetic properties via cation doping for h-$YMnO_3$. However, the incorporation of different ions raises many questions in relation to the preferred sites, the charge-compensating mechanisms, and whether the doping process is energetically favorable, which are intractable in experiment. Our simulation can probe these issues by quantitatively estimating the relative energies of different dopant substitution. Here we examined a variety of dopants from monovalent (M^+) to tetravalent (M^{4+}) ions substituted at Y sites (Two inequivalent yttrium sites Y1 and Y2 are at

the 2a and 4b positions, respectively), which constitute wider theoretical studies than current experimental reports.

For isovalent dopants (M^{3+}), no charge-compensation is required. However, for heterovalent dopants (M^{+}, M^{2+}, M^{4+}), the charge-compensating mechanisms have not been clearly established and can consist of either metal vacancy, O vacancy, or electronic species (e.g., $h^{\cdot}$, e'). Hence these mechanisms are all considered in this work. Our calculation has found that the metal vacancy compensating mechanism is highly unfavorable for h-$YMnO_3$ (the data are not shown here). Thus for the cation doping at the Y site, incorporation mechanisms of the following types (normalized to a single dopant ion) are taken into account by using Kröger-Vink notation:monovalent dopants with oxygen vacancy formation:

$$\tfrac{1}{2}M_2O + Y_Y^{\times} + O_O^{\times} \rightarrow M_Y'' + V_O^{\cdot\cdot} + \tfrac{1}{2}Y_2O_3; \quad (6a)$$

monovalent dopants with hole formation:

$$\tfrac{1}{2}M_2O + Y_Y^{\times} + O_O^{\times} \rightarrow M_Y'' + 2h^{\cdot} + \tfrac{1}{2}Y_2O_3; \quad (6b)$$

divalent dopants with oxygen vacancy formation:

$$MO + Y_Y^{\times} + \tfrac{1}{2}O_O^{\times} \rightarrow M_Y' + \tfrac{1}{2}V_O^{\cdot\cdot} + \tfrac{1}{2}Y_2O_3; \quad (7a)$$

divalent dopants with hole formation:

$$MO + Y_Y^{\times} + \tfrac{1}{2}O_O^{\times} \rightarrow M_Y' + h^{\cdot} + \tfrac{1}{2}Y_2O_3; \quad (7b)$$

trivalent dopants (no compensation):

$$\tfrac{1}{2}M_2O_3 + Y_Y^{\times} \rightarrow M_Y^{\times} + \tfrac{1}{2}Y_2O_3; \quad (8)$$

tetravalent dopants with electron formation:

$$MO_2 + \tfrac{4}{3}Y_Y^{\times} \rightarrow M_Y^{\cdot} + e' + \tfrac{2}{3}Y_2O_3. \quad (9)$$

The interatomic potentials for dopants are obtained from Refs. 41–44. Since there are four inequivalent oxygen sites in the lattice of h-$YMnO_3$, the most probable oxygen vacancy site is found to be the O3 site with the energy of 20.82 eV. Contrary to the case in the $LaMnO_3$ perovskite,[45] our calculation found that the hole ($h^{\cdot}$) preferred to localize at the O1 site (O^{-}) with the energy of 2.10 eV rather than at the Mn site (Mn^{4+}). Such localization of holes has also been found in other compounds, such as $LaGaO_3$.[46] Nevertheless, the electron (e') is likely to localize at the Mn site (Mn^{2+}) with the energy of -0.46 eV. Indeed, optical ellipsometry spectroscopy of h-$YMnO_3$ single crystals has indicated the polaron effects that charge transfers from the oxygen ions to manganese with the formation of a hole in the oxygen ions and the acceptance of an electron of Mn^{3+}.[47] The energies for solution reactions (called solution energies) are calculated by combining these defect, substitutional, and lattice energy terms for each equation. The calculated solution energies for these dopants with different charge-compensating mechanisms are plotted as functions of the ionic radius in Figs. 3(a)–3(d). The values of dopant radii have been taken from Shannon.[48]

Our calculation reveals four main points. First, the calculation shows that all the five M^{4+} dopants have relatively large negative solution energies [Figs. 3(a)–3(d)], indicating that they are possibly easily soluble in h-$YMnO_3$. The Zr^{4+} ion has the lowest solution energy and favors to enter the Y2 site. In $Y_{1-x}Zr_xMnO_3$ ($x < 0.3$), x-ray diffraction (XRD) and energy-dispersive spectroscopy have found no traces of other Zr containing oxides, indicating that the doped Zr^{4+} cations truly entered into the hexagonal phase.[49] Moreover, Rietveld refinement of the XRD patterns further confirmed that the Zr^{4+} was incorporated into the Y site.[49] Sn^{4+} is a less favorable dopant than Zr^{4+}, yet it still has a negative solution energy of about -5 eV. Besides, it seems that Sn^{4+} also has a preference to enter the Y2 site compared with the Y1 site. Ce^{4+}, Pr^{4+}, and Th^{4+} seem to be able to enter both Y1 and Y2 sites, since they have similar negative solution energies for doping at these two sites, and such occupation has also been observed in the Er-doped case based on neutron-diffraction analysis.[13] As the M^{4+} ions which provide electrons for manganese substitute at Y site, the Mn^{3+} will be changed into Mn^{2+} to keep the charge balance according to the compensating mechanism. Such a valence state of Mn^{2+} was not only speculated in Zr-doped h-$YMnO_3$,[9,49] but has also been found in Ce-doped $Y_{1-x}Ce_xMnO_3$ compounds which hold the $P6_3cm$ space group for $x \leqslant 0.10$.[10,11] The generation of Mn^{2+} states will enhance the double-exchange interaction between Mn^{2+} and Mn^{3+} sites, which favors a ferromagnetic configuration.

Second, our results indicate that M^{+} and M^{2+} cations have an energetic preference for the Y2 site rather than the Y1 site in h-$YMnO_3$. Furthermore, the calculation also reveals that hole compensation is much more energetically favorable than oxygen vacancy compensation for M^{+} and M^{2+} dopants [Figs. 3(a) and 3(b)]. This result seems to be compatible with the claim that the presence of oxygen vacancies within the h-$YMnO_3$ structure was unlikely[50] and the result that oxygen was superstoichiometric for h-$YMnO_3$ prepared at ambient atmosphere.[51] Nevertheless, it should be noted that the oxygen content of h-$YMnO_3$ could be varied according to the oxygen partial pressure, and oxygen vacancies may be created in samples prepared at lower oxygen partial pressure.[51] A recent report has shown that phases of $YMnO_{3-x}$ ($0 \leqslant x < 0.2$) can be yielded by topotactic reduction of h-$YMnO_3$ with CaH_2 within the temperature range 498–623 K.[52]

Third, for the monovalent ions, our calculation finds that the most favorable dopant is Na^{+}. It also shows that Li^{+} has a relative favorable energy which is in agreement with the experimental result that Li^{+} can be incorporated into h-$YMnO_3$.[8] In addition, we also find that the most favorable dopant among the studied divalent cations is Ca. Accordingly, Ca^{2+} has been found to substitute for the Y^{3+} site in $Y_{1-x}Ca_xMnO_3$ with a large x over 0.22 while retaining the hexagonal structure,[53] and this x value has been suggested as 0.15 recently.[54]

Finally, our results show that all the M^{3+} dopants under study have positive solution energies, indicating that they are difficult to incorporate into h-$YMnO_3$ or have a quite limited solubility. This is especially true for La^{3+}, Sm^{3+}, and Nd^{3+} cations since they cannot hold hexagonal structure for manganites due to larger ionic radius, and thus their manganites only exist in perovskites. However, a small amount of Lu^{3+}, Ho^{3+}, or Yb^{3+}, which have relatively lower energies, may accommodate the Y2 site due to a similar ionic radius compared with the Y^{3+} ion (0.96 Å) (their stable manganites also share the same hexagonal structures as $YMnO_3$). The substitution of Lu^{3+} for Y^{3+} was reported; nevertheless, the substitution preference for the two distinct Y1 and Y2 sites

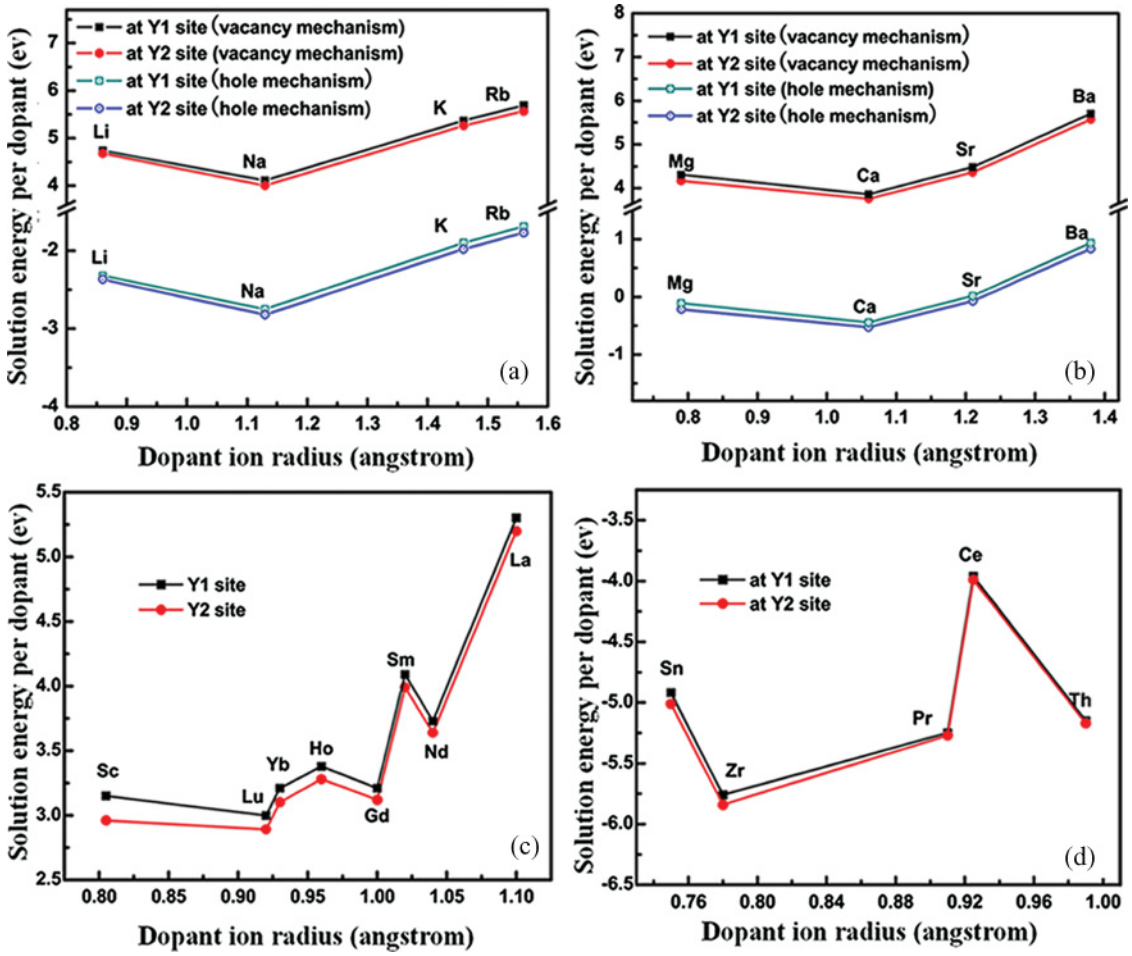

FIG. 3. (Color online) Solution energies at Y site vs dopant ionic radius. Lines are a guide for the eye only. (a) Monovalent dopants, (b) divalent dopants, (c) trivalent dopants, (d) tetravalent dopants.

has not been experimentally determined yet.[14] In the following section, the doping effect of several probable dopants (Zr^{4+}, Sn^{4+}, Ce^{4+}, Th^{4+}, Na^{+}, Ca^{2+}) on the local structure and polarization for *h*-$YMnO_3$ will be discussed. To compare with the role of Y^{3+} in the local structure and the polarization of *h*-$YMnO_3$, the doping of Lu^{3+} and Ho^{3+} are also considered.

C. Local structure and polarization

In contrast to the centrosymmetric paraelectric phase, the Y1 ions go upward and the Y2 ions turn downward along the *c* axis, while in-plane O3 and O4 move oppositely relative to Y1 and Y2, respectively, in the ferroelectric phase [Fig. 4(a)], forming a triangular Y plane buckled with MnO_5 bipyramids. The buckling of the Y plane can be represented by the difference of the *z* position of the two inequivalent Y ions, $Y1(z) - Y2(z)$.[9] In addition, a small tilting of MnO_5 bipyramids toward O3 has also been observed at the trigonal oxygen plane in this structure [Figs. 1 and 4(a)]. The magnitude of tilting of MnO_5 polyhedra from the *ab* basal plane can be represented by the angle between the O3-O4 bond and the *ab* basal plane.

It is interesting to examine the local structural changes caused by cation doping. Above all, the doping at the Y2 site was first taken into account since most of the studied dopants preferentially enter the Y2 site (Fig. 3). Previous analysis on *h*-$YMnO_3$ revealed that the dominant components of ferroelectric structural distortion was along the *c* axis,[3,9] and thus the calculated changes of *z* coordinates of ions nearest to the dopant are presented in Table III. The detailed ion displacements caused by the doping of Zr^{4+}, Sn^{4+}, Ce^{4+}, and Th^{4+} are schematically shown in Fig. 4(d), while the changes led by Na^{+} and Ca^{2+} are given in Fig. 4(e). For all these dopants, the dominant displacement of ions is for O4*, which is directly below the dopant *M*, moving downward remarkably in the *z* direction (Table III). Nevertheless, the dopant goes upward along the *c* axis from the original Y2 site [Figs. 4(d) and 4(e)]. This motion of the two ions leads to a substantial increase of the *M*-O4* bond length, which elongates by more than 11.89% compared with the original Y2-O4 bond, as listed in Table III. The incorporation of these tetravalent dopants into the Y2 site leads to O3, O4, and the nearest Y2 moving upward, while the nearest Y1 displaces downward [Fig. 4(d)]. Instead, the substitution of Na^{+} and Ca^{2+} results in reversed displacements: O3, O4, and the nearest Y2 move downward while the nearest Y1 goes upward [Fig. 4(e)]. It is notable from Table III that the doping of Lu^{3+}, Ho^{3+}, Ce^{4+}, and Th^{4+}, which share a similar radius with Y^{3+}, results in much smaller displacements than those led by much larger dopants such as Na^{+} and Ca^{2+} or much smaller dopants such as Zr^{4+} and Sn^{4+}. These displacements shorten the Y2-O4 bond. Nevertheless,

TABLE III. Calculated changes of z coordinates of ions next to the doping site (Δz, $\times 10^{-2}$ Å) and bond lengths (Δ_b, in %) for cation doping at Y2 site. Positive Δz indicate upward ionic displacement, while negative Δz indicate downward displacement. Positive Δ_b indicate elongation and negative Δ_b indicate shortening of bond. Note that the mean changes of Δz and Δ_b for all atoms in the system depend on the percentage of doping and they are far less than the data given.

Dopants	Δz	M	O4*	Y2	Y1	O3	O4	Δ_b	M-O4*	Y2-O4	Y1-O3
Na		8.29	−42.50	−9.71	6.08	−7.46	−8.89		19.69	−0.19	4.16
Ca		7.56	−36.24	−5.57	2.31	−3.86	−3.60		16.96	−0.78	1.73
Lu		6.54	−29.57	−0.49	−2.41	0.84	1.96		14.04	−0.97	−0.97
Ho		5.62	−25.16	−1.05	−1.44	0.07	1.05		11.89	−0.97	−0.39
Ce		4.50	−18.35	1.83	−3.89	2.50	4.04		8.91	−0.84	−1.93
Th		3.69	−11.94	0.53	−2.22	1.06	2.48		6.10	−0.75	−0.99
Zr		8.45	−37.43	3.99	−7.92	5.77	7.35		17.86	−1.29	−4.13
Sn		8.18	−37.74	3.63	−7.90	1.45	7.15		17.89	−1.36	−4.07

the changes of the Y1-O3 bond are somewhat complicated: it elongates with Na^+ and Ca^{2+} entering the Y2 site (especially for Na^+), whereas it shortens via other cations doping with the largest shrink for Zr^{4+} and Sn^{4+}. It is worth noting that Na^+ and Ca^{2+} doping yields some contrasted structural changes with those caused by Zr^{4+} and Sn^{4+}, not only for the displacements of Y1, Y2, O3, and O4, but also for the changes of the Y1-O3 bond (Table III). Moreover, unlike the shortening of both the Y1-O3 and Y2-O4 bonds led by other cations (such shortening of Y1-O3 and Y2-O4 via Lu^{3+} substitution has also been found by Van Aken *et al.*[55]), Na^+ and Ca^{2+} doping cause shortening of Y2-O4 but elongation of Y1-O3. It should be mentioned that the defect calculations are at the dilute limit, in which an isolated ion is inserted into the lattice. Thus these values do not correspond to the average changes for all the atoms in this system, which depend on the percentage of doping and are considerably smaller than the displacements here.

The incorporation of cations into the Y1 site was also examined, since these doping actions were likely to take effect. Table IV gives the changes in z coordinates of ions nearest to the dopant. The ion displacements caused by cation doping are schematically shown in Figs. 4(b) and 4(c). In contrast with the upward displacement of the dopant M for doping at the Y2 site, these dopants displace downward when entering the Y1 site [Figs. 4(b)–4(d) and Tables III and IV]. The entrance of the trivalent and tetravalent dopants into the Y1 site push the neighboring Y2 and O4 upward except in the Ho-doped case, which causes O4 to be displaced downward slightly. On the contrary, the O3 goes downward with the exception of the Th-doped case [Fig. 4(b)] and Table IV]. All the ions of the unit have downward displacements when Na^+ and Ca^{2+} enter the Y1 site, as schematically shown in Fig. 4(c). In sharp contrast to the case of Y2-site doping in which the M-O4* bond becomes elongated, the M-O3* bond shortens accompanying doping by these dopants, with the larger shrinkage led by the biggest cations Na^+ and Ca^{2+}, and also the smallest dopants Zr^{4+} and Sn^{4+}. The trivalent and tetravalent dopants have less effect on the Y2-O4 bond than Na^+ and Ca^{2+} which lead to a relatively larger elongation of this bond.

Of further interest in structure, changes of local polyhedron distortion have also been considered. The tilting angle of undoped h-$YMnO_3$ was calculated at about 7.08°, which

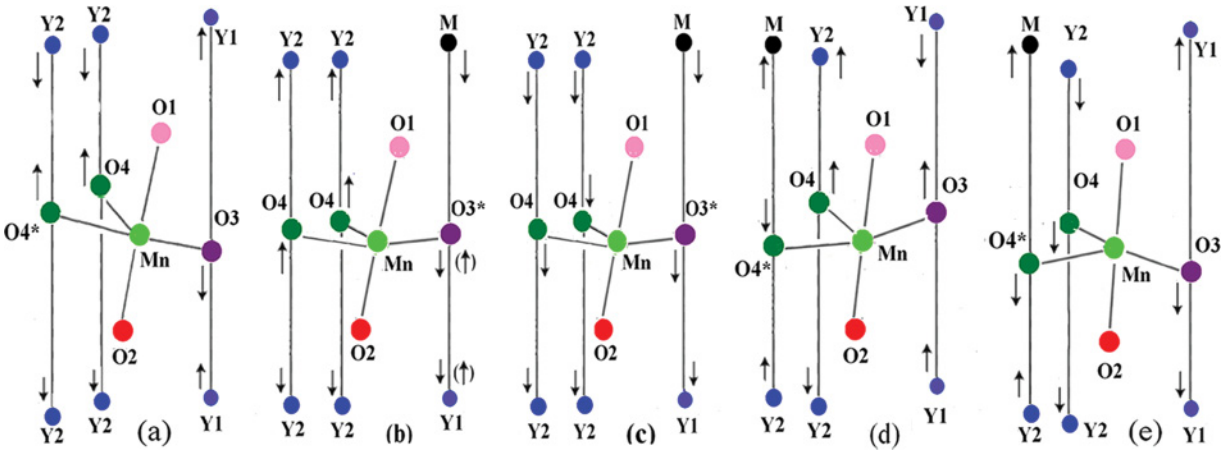

FIG. 4. (Color online) Schematics of a MnO_5 polyhedron with Y layers above and below. The arrows indicate atomic displacements. (a) Atomic displacements of ferroelectric phase in h-$YMnO_3$ compared with centrosymmetric paraelectric phase. (b) Doping at Y1 site with Zr^{4+}, Sn^{4+}, Ce^{4+}, Th^{4+} cations. Note that the Th^{4+} doping leads to upward displacement of O3∗ and Y1 (arrows in brackets), and the Ce^{4+} doping also makes Y1 go upward. (c) Doping at Y1 site with Na^+, Ca^{2+} cations. (d) Doping at Y2 site with Zr^{4+}, Sn^{4+}, Ce^{4+}, Th^{4+} cations. (e) Doping at Y2 site with Na^+, Ca^{2+} cations.

TABLE IV. Calculated changes of z coordinates of ions next to the doping site (Δz, $\times 10^{-2}$ Å) and bond lengths (Δ_b, in %) for cation doping at Y1 site. Positive Δz indicate upward ionic displacement, while negative Δz indicate downward displacement. Positive Δ_b indicate elongation and negative Δ_b indicate shortening of bond. Note that the mean changes of Δz and Δ_b for all atoms in the system depend on the percentage of doping and they are far less than the data given.

Dopants	Δz	M	O3*	Y2[a]	O4[a]	Δ_b	M-O3*	Y2-O4[a]
Na		−13.00	−8.61	−0.62	−14.05		−8.35	5.24
Ca		−10.53	−5.57	−0.43	−6.42		−6.22	2.34
Lu		−8.26	−3.86	0.97	0.46		−4.68	0.20
Ho		−7.80	−2.93	0.65	−0.26		−4.14	*t*0.35
Ce		−6.44	−0.96	1.35	3.26		−2.86	−0.73
Th		−6.22	1.60	0.76	2.00		−1.79	−0.48
Zr		−12.21	−4.70	3.33	5.78		−6.53	−0.93
Sn		−11.01	−4.33	4.01	5.69		−5.92	−0.63

[a]Another Y2 and O4 schemed in Figs. 4(b) and 4(c) which have the same changes as those in Table IV are not listed again.

is in excellent agreement with the experimental data.[9] Incorporation of these dopants into the Y2 site reduces this angle, and the largest reduction is caused by the smallest dopants Sn^{4+} and Zr^{4+}, rather than by the largest cation Na^{+} [Fig. 5(c)]. Although the Na^{+} dopant still gives the smallest tilting angle among the studied dopants when they occupy the Y1 site, it is much larger than that caused by Y2-site doping [Figs. 5(a) and 5(c)]. The occupation of Ho^{3+}, Lu^{3+}, Ce^{4+}, Th^{4+}, Zr^{4+}, and Sn^{4+} at the Y1 site enhances the tilting, with the largest values yielded by the smallest dopants, Zr^{4+} and Sn^{4+}. For the buckling, it seems that it increases with the increasing dopant radius generally when these dopants enter the Y2 site. In contrast to the suppression of buckling by other dopants, the substitution of Na^{+} and Ca^{2+} enhance the buckling, especially for Na^{+} [Fig. 5(d)], whereas for the doping at the Y1 site, these studied dopants all suppress the buckling. The suppression of tilting of MnO_5 polyhedra and buckling of the Y plane caused by smaller dopants has been found in the x-ray-diffraction pattern, where the peaks arising from such distortion drastically decrease in their intensity with

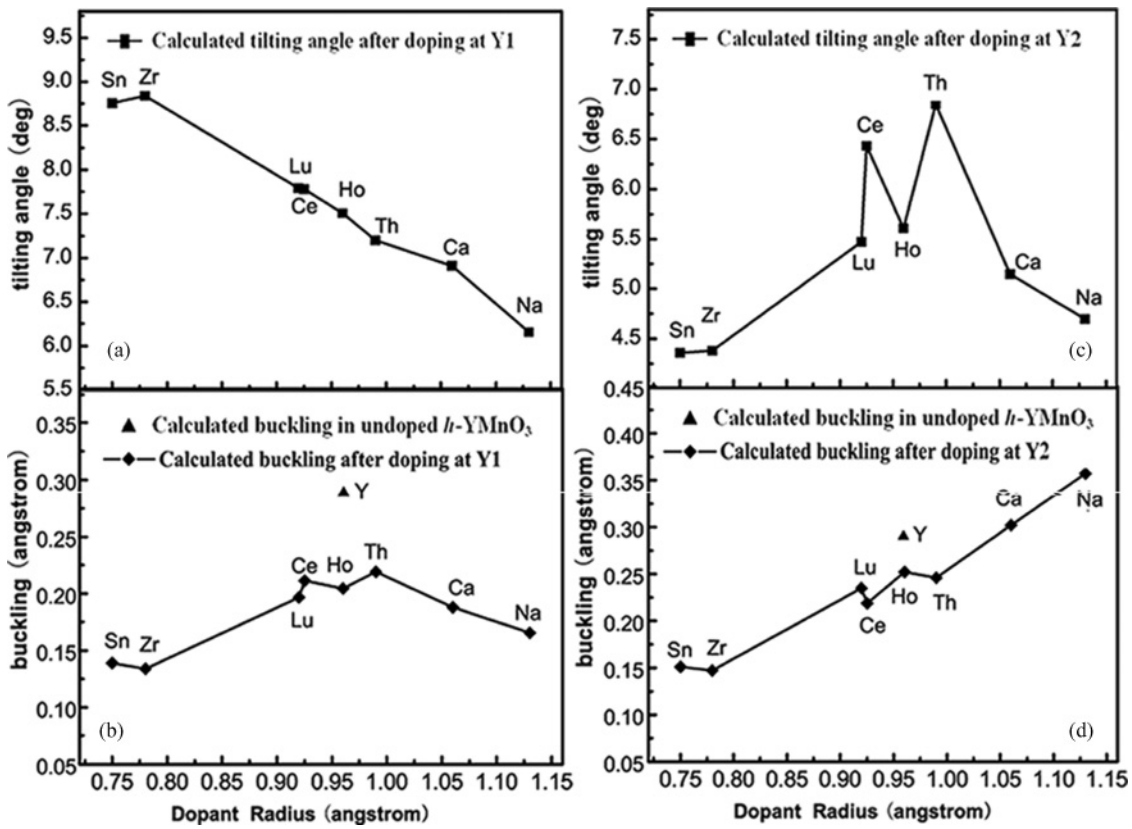

FIG. 5. Tilting angle of MnO_5 polyhedron from *ab* basal plane (a) and the magnitude of the Y buckling (b) against dopant radius for doping at Y1 and Y2 site. The ▲ symbol in (b) and (d) denotes the calculated original value of buckling in undoped *h*-$YMnO_3$. The calculated original tilting angle in undoped *h*-$YMnO_3$ is 7.08°, which agrees well with the experimental data from Ref. 9.

TABLE V. Calculated changes of local polarization (ΔP, $\mu C/cm^2$) for cation doping at Y1 and Y2 sites along x, y, and z for a $1 \times 1 \times 2$ supercell $Y_{36}Mn_{36}O_{108}$, which is a hexagonal prism with $a = 6.12$ Å and $c = 22.86$ Å. For comparison, part of them adopt scientific notation (accuracy limit 0.0001 $\mu C/cm^2$).

	Doping site Y2 (4b)			Doping site Y1 (2a)		
	ΔP_z	ΔP_x	ΔP_y	ΔP_z	ΔP_x	ΔP_y
Na	−0.6486	-0.54×10^{-2}	1.0×10^{-2}	−0.8487	0	−0.7787
Ca	−0.5479	-0.29×10^{-2}	0.57×10^{-2}	−0.1813	0	−0.4136
Lu	−0.4171	-0.06×10^{-2}	0.10×10^{-2}	0.1236	0	-3.58×10^{-2}
Ho	−0.3437	-0.02×10^{-2}	0.03×10^{-2}	0.1133	0	-2.11×10^{-2}
Ce	−0.3155	-0.09×10^{-2}	0.02×10^{-2}	0.2423	0	0.3670
Th	−0.2787	-0.11×10^{-2}	0.03×10^{-2}	0.2463	0	0.3878
Zr	−0.6105	0.15×10^{-2}	-0.39×10^{-2}	0.3870	0.03×10^{-2}	0.3095
Sn	−0.6184	0.15×10^{-2}	-0.41×10^{-2}	0.3122	0.09×10^{-2}	0.3375

Zr doping.[9] It seems that our calculated result is controversial compared with the reported experimental result,[9] since Zr^{4+} doping at the Y1 site enhances the tilting notably [Fig. 5(a)]. Nevertheless, the calculated result has indicated that the Zr^{4+} dopant preferentially enters the Y2 site [Fig. 3(d)], which suppresses the tilting significantly [Fig. 5(c)].

The simulation also provides information on the changes in local ferroelectric polarization via cation doping. The overall polarization of undoped h-$YMnO_3$ crystal was defined as P_0. In the calculation, the changes of local polarization of the calculated cell (ΔP) was determined from the core-shell displacements and the displacements of the ions (Δr) from their reference positions.[28,38] The α ($\alpha = x, y, z$) Cartesian component of ΔP of the calculated cell can be defined as[28,38]

$$\Delta P_\alpha = \sum_i (q_{ic} \Delta r_{ic\alpha} + q_{is} \Delta r_{is\alpha}), \tag{10}$$

where ic and is correspond to the core and shell of a given ion i, and the sum on i runs over the ions in the stoichiometric cell. The cell used for the calculation can be defined in several ways, and here we take the doping site as the center of the supercell with a stoichiometry $Y_{36}Mn_{36}0_{108}$. The supercell was $1 \times 1 \times 2$ along a, b, c directions, that is, a hexagonal prism with $a = 6.12$ Å and $c = 22.86$ Å. Table V shows the calculated ΔP via cation doping. When doping at the Y2 site, the changes of local polarization occur mainly along the c axis, which are about two orders of magnitude larger than those in the plane. This result seems to be compatible with the result of spontaneous polarization in h-$YMnO_3$ generated along the c axis of the crystal.[3,9] Thus the changes of planar polarization ($\Delta P_x, \Delta P_y$) resulting from cation doping at the Y2 site can be ignored for simplicity. Negative values of ΔP ($\Delta P \approx \Delta P_z$) for the eight dopants indicate that incorporation of these cations reduces the overall polarization, especially for Na^+, Sn^{4+}, Zr^{4+}, and Ca^{2+}, and the smallest effect is for the dopants which share a similar radius with Y^{3+}, such as Th^{4+}, Ce^{4+}, Ho^{3+} (Table V). Contrarily, for the incorporation of the tetravalent dopants and Na^+ and Ca^{2+} into the Y1 site, ΔP_y shows a remarkable difference from that of the Y2-site doping despite that ΔP_x is still nearly zero. Local polarization generates along the y forward direction for the tetravalent dopants, whereas Na^+ and Ca^{2+} cause reversed ΔP_y. Besides, Na^+ and Ca^{2+} also suppress the polarization in the z direction, as in the case of Y2-site doping. Nevertheless, the trivalent and tetravalent dopants enhance the P_z. It is also interesting to find that for the doping of trivalent Lu^{3+} and Ho^{3+} the changes of polarization are mainly along the c axis and with very small or zero ΔP_x and ΔP_y. Compared to the changes of local polarization (Table V) caused by Lu^{3+} and Ho^{3+} with those resulting from Ce^{4+} and Th^{4+}, which all share a similar radius with each other ($Lu^{3+} \sim 0.92$ Å, $Ce^{4+} \sim 0.925$ Å, $Ho^{3+} \sim 0.96$ Å, $Th^{4+} \sim 0.99$ Å), the calculated result seems to support the proposal[3] that electrostatic effect indeed affected the polarization.

Several reports have revealed that the tilting of MnO_5 bipyramids and the buckling of Y layers are responsible for spontaneous electric polarization.[3,9] We note that the changes of polarization ΔP seem to be correlated with the changes of the tilting of the MnO_5 polyhedron upon doping of these cations, as shown in Figs. 5(a) and 5(c) and Table V. The suppression of the tilting of MnO_5 bipyramids caused by cation doping corresponds to the reduction of polarization, which is compatible with the result derived under magnetic field that reduction of MnO_5 tilting decreased the polarization.[56] Besides, the experimental result that ferroelectric polarization of h-$YMnO_3$ was suppressed by Zr^{4+} doping[9] seems to support the calculated result that Zr^{4+} preferentially occupies the Y2 site, which reduces the polarization significantly, rather than entering the Y1 site, which enhances the polarization [Fig. 3(d)] and Table V]. Our calculation revealed that Zr^{4+}, Sn^{4+}, Na^+, and Ca^{2+} are "deleterious" dopants for ferroelectric polarization, while the doping effects of Ce^{4+} and Th^{4+} on polarization need further confirmation. In addition, it should be stressed that the final ferroelectric properties of the doped h-$YMnO_3$ are also influenced by other factors, such as leakage current resulting from the charge compensation of heterovalent dopants. It is therefore difficult to relate the local polarization to the final ferroelectric properties of the doped crystal, and experimental investigation is needed.

It has been still controversial for the driving force of ferroelectric polarization in h-$YMnO_3$. Based on density-functional theory calculation, Aken *et al.* claimed that the ferroelectric polarization from the displacement of Y^{3+} and O3 (O4) was driven entirely by electrostatic and size effects.[3] This standpoint was supported by the subsequent calculation of isostuctural $ReGaO_3$ and $ReInO_3$ (where Re stands for

rare-earth ions).[57] Our calculation shows that electrostatic and size effects do have an effect on the ferroelectric polarization. Nevertheless, we also note that although Lu^{3+} and Ho^{3+} have a similar ionic radius and the same charges as Y^{3+}, they still lead to different structural and polarization changes compared to those of *h*-$YMnO_3$ (Tables III–V). It appears that the ferroelectric polarization from the displacement of Y^{3+} and O3 (O4) may be not driven entirely by electrostatic and size effects. Some other factors may also play a role. For example, first-principle calculation suggested that the Y d^0-ness with rehybridization was the driving force for the ferroelectric polarization,[58] while some researchers have proposed that Mn trimerization is related to the polarization.[6,59] More studies are required to further clarify this point.

IV. CONCLUSION

The interatomic potentials of multiferroic *h*-$YMnO_3$ have been developed, which can reproduce its crystal structure quite well. The doping behaviors of a variety of dopants from monovalent to tetravalent ions at the Y site have been systematically investigated by employing atomistic simulation techniques. It is found that Zr^{4+}, Sn^{4+}, Na^{+}, and Ca^{2+} are the favorable dopants to incorporate into *h*-$YMnO_3$ and preferentially enter the Y2 site, while Ce^{4+} and Th^{4+} can enter both Y1 and Y2 sites. The structural changes and local polarization caused by these dopants are also investigated. The incorporation of the studied dopants into the Y2 site suppresses the tilting of the MnO_5 polyhedron, while the incorporation of these dopants into the Y1 site enhances the tilting except for Na^{+} and Ca^{2+}. It is also found that Zr^{4+}, Sn^{4+}, Na^{+}, and Ca^{2+} are deleterious dopants for ferroelectric polarization. We also find that the ferroelectric polarization of *h*-$YMnO_3$ is not driven entirely by electrostatic and size effects, although they have an important influence.

ACKNOWLEDGMENTS

We are grateful to F. L. Tang for his helpful discussions. We would like to acknowledge the financial support by The National Science Foundation of China (Grants No. U0734001 and No. 50772054) and The Ministry of Science and Technology of China (Grant No. 2009CB929202).

*Author to whom correspondence should be addressed. xzzhang@tsinghua.edu.cn

[1] W. Prellier, M. P. Singh, and P. Murugavel, J. Phys.: Condens. Matter **17**, R803 (2005).
[2] W. Eerenstein, N. D. Mathur, and J. F. Scott, Nature (London) **442**, 759 (2006).
[3] B. B. Van Aken, T. T. M. Palstra, A. Filippetti, and N. A. Spaldin, Nature Mater. **3**, 164 (2004).
[4] S. Lee, A. Pirogov, M. Kang, K. H. Jang, M. Yonemura, T. Kamiyama, S.-W. Cheong, F. Gozzo, N. Shin, H. Kimura, Y. Noda, and J. G. Park, Nature (London) **451**, 805 (2008).
[5] S. C. Abrahams, Acta Crystallogr., Sect. B **57**, 485 (2001).
[6] T. Choi, Y. Horibe, H. T. Yi, Y. J. Choi, W. D. Wu, and S.-W. Cheong, Nature Mater. **9**, 253 (2010).
[7] T. Shimura, N. Fujimura, S. Yamamori, T. Yoshimura, and T. Ito, Jpn. J. Appl. Phys. **37**, 5280 (1998).
[8] N. Fujimura, H. Sakata, D. Ito, T. Yoshimura, T. Yokota, and T. Ito, J. Appl. Phys. **93**, 6990 (2003).
[9] T. Katsufuji, M. Masaki, A. Machida, M. Moritomo, K. Kato, E. Nishibori, M. Takata, M. Sakata, K. Ohoyama, K. Kitazawa, and H. Takagi, Phys. Rev. B **66**, 134434 (2002).
[10] S. K. Srivastava, M. Kar, S. Ravi, P. K. Mishra, and P. D. Babu, J. Magn. Magn. Mater. **320**, 2382 (2008).
[11] K. Hirota, K. Fujita, M. Yoshinaka, and O. Yamaguchi, J. Mater. Sci. **40**, 801 (2005).
[12] T. Choi, and J. Lee, Appl. Phys. Lett. **84**, 5043 (2004).
[13] M. C. Sekhar, S. Lee, G. Choi, C. Lee, and J.-G. Park, Phys. Rev. B **72**, 014402 (2005).
[14] J. Park, S. Lee, M. Kang, K.-H. Jang, C. Lee, S. V. Streltsov, V. V. Mazurenko, M. V. Valentyuk, J. E. Medvedeva, T. Kamiyama, and J.-G. Park, Phys. Rev. B **82**, 054428 (2010).
[15] S. Mori, J. Tokunaga, Y. Horibe, Y. Aikawa, and T. Katsufuji, Phys. Rev. B **72**, 224434 (2005).
[16] U. Adem, A. A. Nugroho, A. Meetsma, and T. T. M. Palstra, Phys. Rev. B **75**, 014108 (2007).
[17] A. A. Nugroho, N. Bellido, U. Adem, G. Nénert, Ch. Simon, M. O. Tjia, M. Mostovoy, and T. T. M. Palstra, Phys. Rev. B **75**, 174435 (2007).
[18] J. Park, M. Kang, J. Kim, S. Lee, K.-H. Jang, A. Pirogov, J.-G. Park, C. Lee, S. H. Park, and H. C. Kim, Phys. Rev. B **79**, 064417 (2009).
[19] C. Parker and G. D. Price, in *Computer Modeling of Fluids, Polymers and Solids*, Vol. 293 of NATO Advanced Study Institute, edited by C. R. A. Catlow, S. C. Parker, and M. P. Allen (Springer, New York, 1988), p. 405.
[20] C. R. A. Catlow, in *Solid State Chemistry—Techniques*, edited by A. K. Cheetham and P. Day (Clarendon, Oxford, 1987), p. 231.
[21] B. G. Dick and A. W. Overhauser, Phys. Rev. **112**, 90 (1958).
[22] N. F. Mott and M. T. Littleton, Trans. Faraday Soc. **34**, 485 (1938).
[23] J. Gale and A. L. Rohl, Mol. Simul. **29**, 291 (2003).
[24] X. Zhang and C. R. A. Catlow, Phys. Rev. B **46**, 457 (1992).
[25] X. Zhang and C. R. A. Catlow, Phys. Rev. B **47**, 5315 (1993).
[26] X. Zhang, K. W. Yip, and C. K. Ong, Phys. Rev. B **51**, 1277 (1995).
[27] X. Zhang and C. K. Ong, Phys. Rev. B **48**, 6865 (1993).
[28] M. Sepliarsky, S. R. Phillpot, D. Wolf, M. G. Stachiotti, and R. L. Migoni, J. Appl. Phys. **90**, 4509 (2001).
[29] M. Sepliarsky, M. G. Stachiotti, and R. L. Migoni, Phys. Rev. Lett. **96**, 137603 (2006).
[30] S. Tinte and M. G. Stachiotti, Phys. Rev. B **64**, 235403 (2001); M. Sepliarsky, M. G. Stachiotti, and R. L. Migoni, *ibid.* **72**, 014110 (2005).
[31] N. N. Kovaleva, A. V. Boris, L. Capogna, J. L. Gavartin, P. Popovich, P. Yordanov, A. Maljuk, A. M. Stoneham, and B. Keimer, Phys. Rev. B **79**, 045114 (2009).

[32]R. Choithrani, M. N. Rao, S. L. Chaplot, N. K. Gaur, and R. K. Singh, New J. Phys. **11**, 073041 (2009).
[33]M. N. Iliev, H.-G. Lee, V. N. Popov, M. V. Abrashev, A. Hamed, R. L. Meng, and C. W. Chu, Phys. Rev. B **56**, 2488 (1997).
[34]M. Zaghrioui, V. Ta Phuoc, R. A. Souza, and M. Gervais, Phys. Rev. B **78**, 184305 (2008).
[35]M. N. Rao, N. Kaur, S. L. Chaplot, N. K. Gaur, and R. K. Singh, J. Phys.: Condens. Matter **21**, 355402 (2009).
[36]E. G. Rini, M. N. Rao, S. L. Chaplot, N. K. Gaur, and R. K. Singh, Phys. Rev. B **75**, 214301 (2007).
[37]F. L. Tang and X. Zhang, Phys. Rev. B **73**, 144401 (2006).
[38]S. Lee, A. Pirogov, J. H. Han, J.-G. Park, A. Hoshikawa, and T. Kamiyama, Phys. Rev. B **71**, 180413 (2005).
[39]D. P. Kozlenko, S. E. Kichanov, S. Lee, J.-G. Park, V. P. Glazkov, and B. N. Savenko, JETP Lett. **82**, 193 (2005).
[40]M. Janoschek, B. Roessli, L. Keller, S. N. Gvasaliya, K. Conder, and E. Pomjakushina, J. Phys.: Condens. Matter **17**, L425 (2005).
[41]M. S. D. Read, M. S. Islam, G. W. Watson, F. King, and F. E. Hancock, J. Mater. Chem. **10**, 2298 (2000).
[42]G. V. Lewis and C. R. A. Catlow, J. Phys. C **18**, 1149 (1985).
[43]C. A. J. Fisher, V. M. Hart Prieto, and M. S. Islam, Chem. Mater. **20**, 5907 (2008).
[44]C. Milanese, V. Buscaglia, F. Maglia, and U. A. Tamburini, Chem. Mater. **16**, 1232 (2004).
[45]R. A. De Souza, M. S. Islam, and E. Ivers-Tiffée, J. Mater. Chem. **9**, 1621 (1999).
[46]M. S. Khan, M. S. Islam, and D. R. Bates, J. Phys. Chem. B **102**, 3099 (1998).
[47]A. M. Kalashnikova and R. V. Pisarev. JETP Lett. **78**, 143 (2003).
[48]R. D. Shannon, Acta Crystallogr., Sect. A **32**, 751 (1976).
[49]B. B. Van Aken, Jan-Willem G. Bos, R. A. de Groot, and T. T. M. Palstra, Phys. Rev. B **63**, 125127 (2001).
[50]G. Ńenert, M. Pollet, S. Marinel, G. R. Blake, A. Meetsma, and T. T. M. Palstra, J. Phys.: Condens. Matter **19**, 466212 (2007).
[51]K. Kamata, T. Nakajima, and T. Nakamura, Mater. Res. Bull. **14**, 1007 (1979).
[52]A. J. Overton, J. L. Best, I. Saratovsky, and M. A. Hayward, Chem. Mater. **21**, 4940 (2009).
[53]C. Moure, M. Villegas, J. F. Fernandez, J. Tartaj, and P. Duran, J. Mater. Sci. **34**, 2565 (1999).
[54]A. G. Razumnaya, A. G. Rudskaya, M. F. Kupriyanov, and Y. V. Kabirov, Phys. Solid State **51**, 2304 (2009).
[55]B. B. Van Aken and T. T. M. Palstra, Phys. Rev. B **69**, 134113 (2004).
[56]A. K. Singh, S. Patnaik, S. D. Kaushik, and V. Siruguri, Phys. Rev. B **81**, 184406 (2010).
[57]T. Tohei, H. Moriwake, H. Murata, A. Kuwabara, R. Hashimoto, T. Yamamoto, and I. Tanaka, Phys. Rev. B **79**, 144125 (2009).
[58]D.-Y. Cho, J.-Y. Kim, B.-G. Park, K.-J. Rho, J.-H. Park, H.-J. Noh, B. J. Kim, S.-J. Oh, H.-M. Park, J.-S. Ahn, H. Ishibashi, S.-W. Cheong, J. H. Lee, P. Murugavel, T. W. Noh, A. Tanaka, and T. Jo, Phys. Rev. Lett. **98**, 217601 (2007).
[59]Y. Aikawa, T. Katsufuji, T. Arima, and K. Kato, Phys. Rev. B **71**, 184418 (2005).